Nb-doped Rutile TiO_2 Nanorods for Lithium-ion Batteries

Aleksandra J. Gardecka,[1,2] Mechthild Lübke,[1,2] Ceilidh F. Armer,[2,3] Ding Ning,[2]

M.V. Reddy,[4,5] Adrian Lowe,[3] Zhaolin Liu,[2] Jawwad A. Darr,[1] Ivan P. Parkin[1]

[1] Department of Chemistry, University College London, 20 Gordon Street, London, WC1H 0AJ, UK
[2] Institute of Materials Research and Engineering (IMRE), A*STAR (Agency for Science, Technology and Research), 2 Fusionopolis Way, Innovis #08-03, Singapore 138634, Republic of Singapore.
[3] College of Engineering and Computer Science, Australian National University, Canberra, ACT 0200, Australia
[4] Department of Physics, National University of Singapore, Singapore 117542
[5]Department of Materials Science and Engineering, National University of Singapore, Singapore 117576

Abstract

Pristine and Nb-doped (3.5 at%) rutile TiO_2 materials were synthesized via a hydrothermal method and investigated as possible negative electrode materials for lithium-ion batteries. The materials were characterized via a range of analytical techniques including powder X-ray diffraction, X-ray photoelectron spectroscopy, scanning electron microscopy, transmission electron microscopy and Brunauer-Emmett-Teller surface area measurements. A comprehensive study with potentiodynamic and galvanostatic methods was applied in order to understand the excellent and superior performance of the Nb-doped rutile phase of TiO_2 compared to the undoped counterpart. Cycling between 1-3 V *vs* Li/Li^+ showed that Nb^{5+} doping results in higher capacities mainly due to the smaller particle size, optimized surface area and orientation of the nanorods. For cycling between 0.05-3 V *vs* Li/Li^+, the introduction of Nb^{5+} promotes a higher conversion of rutile TiO_2 from the lithiated to de-lithiated state. After 100 cycles at 100 mA g^{-1}, the Nb-doped rutile TiO_2 maintains a capacity of 390 mAh g^{-1}, 64% higher than undoped TiO_2.

Keywords: hydrothermal, TiO_2, rutile, doping, niobium, lithium ion battery

Graphical Abstract

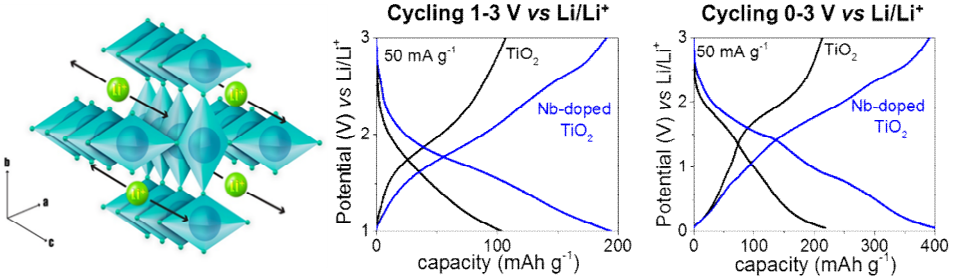

1. Introduction

Lithium-ion batteries can display characteristics of high energy density and long cycle life, which makes them attractive for a range of applications from portable electronic devices to electric vehicles [1]. A lithium-ion battery consists of a negative electrode (conventionally carbon/graphite) and positive electrode (*e.g.* $LiCoO_2$, $LiFePO_4$) which are kept apart by a separator that is soaked with an electrolyte, typically a $LiPF_6$ salt in a mixture of organic solvents [2-4].

Current electrode material research has focused on obtaining nanoscale materials (in particular, two-dimensional nanomaterials, such as nanorods, continuous nanofibers, or nanowires) with high surface area and specific particle morphologies which are known to enhance the lithium-ion diffusion [5, 6]. These materials can readily be made on a laboratory scale using well established synthesis approaches such as batch hydrothermal or solvothermal syntheses [7, 8]. Hydrothermal syntheses allow particles with well-defined morphologies and reduced aggregation [9-11]. Such nanomaterials are often obtained at higher purities than those of their precursors [12].

Titanium dioxide is a candidate negative electrode material due to its low cost, environmental inertness, lithium-ion storage capability, long cycle life and durability [11, 13]. The lithium-ion insertion and de-insertion of rutile TiO_2 is highly anisotropic into the 1D channels, *e.g.* the lithium-ion diffusion is fast along the *c*-axis and it proceeds very slowly in the *ab*-plane [14]. Experimental studies and simulations showed that the lithium-ion diffusion coefficient along the *c*-axis was approximately 10^{-6} cm^2 s^{-1} whereas it was only 10^{-15} cm^2 s^{-1} in the *ab*-plane [15-18]. In micron-sized rutile TiO_2 the very slow diffusion in the *ab*-plane hinders lithium-ion access to the thermodynamically favorable octahedral sites. Comparable to $LiFePO_4$, lithium-ion pairs can block the *c*-channels and prevent further lithiation because of the poor diffusion in the *ab*-plane [15, 19]. Moreover, it has been shown that the amount of stored lithium-ions in

the rutile host is directly related to particle morphology and size characteristics. For bulk rutile TiO_2, only 0.03 mol of lithium-ions (*ca.* 30 mAh g^{-1}) can be stored at an applied current of 30 mA g^{-1} (*ca.* 11 h), whereas nanosizing can drastically increase the solubility of lithium-ions in the rutile structure [20-22]. Therefore, the main strategy for optimizing the electrochemical performance of rutile TiO_2 is to substantially decrease the particle size, with the *c*-axis exposed to the electrolyte and increased unit cell parameters facilitating higher lithium-ion kinetics. This can be achieved by doping TiO_2 with Nb^{5+} into the structure as Nb^{5+} has larger atomic radius than Ti^{4+} (0.0640 nm and 0.0603 nm, respectively) and substitutional doping of Nb^{5+} into TiO_2 lattice has been shown to result in the expansion of whole unit cell [23]. Doping Nb^{5+} into the TiO_2 lattice improves other properties useful for lithium-ion battery applications, such as increased electrical conductivity, maintenance of a wide band gap (from 3.20 eV for anatase and 3.03 eV for rutile [24]), smaller crystal sizes with higher surface areas than in the pristine material, whilst maintaining similar mechanical and chemical stability [25].

It is generally accepted that the first lithium-ion insertion into rutile TiO_2 is composed of three lithiation steps (Figure 1) [20, 21]. The first domain is between 3 to *ca.* 1.45 V *vs* Li/Li^+ and could be assigned to a solid solution reaction [20] which is a result of lithium-ion surface storage on high surface area rutile TiO_2 [21]. The second domain is at *ca.* 1.4 V *vs* Li/Li^+ and can be assigned to another reversible solid solution reaction where the lithium-ion might occupy the octahedral position in the *ab*-plane [15, 17, 20, 21]. The third domain is below 1.4 V *vs* Li/Li^+ and could be assigned to a biphasic transition which is irreversible and results in significant decrease in crystallite size [20, 21]. There are reports concluding the formation of rock salt $LiTiO_2$ during the last irreversible lithiation plateau [20, 26, 27]. This was in disagreement with other reports arguing the formation of lamellar hexagonal $LiTiO_2$ [21, 28] or monoclinic $LiTiO_2$ (P2/m, space group 10; similar to the hexagonal structure) [29].

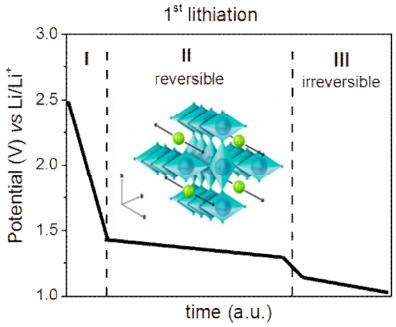

Figure 1: Scheme of the initial lithiation curve for a galvanostatic measurement applied on rutile electrode materials in the potential range of 1 to 3 V *vs* Li/Li^+.

In the majority of studies, TiO_2 has been found to be only electrochemically active between 1.0 to 1.7 V *vs* Li/Li^+ (redox activity of Ti^{3+}/Ti^{4+}), with a maximum theoretical capacity of 336 mAh g^{-1} (reduced to $LiTiO_2$) [19]. However there have been many recent reports showing huge capacity wins at lower potentials between 0.05 to 1 V *vs* Li/Li^+ [30-34]. The origin of this expanded electrochemical activity in a wider potential window might be additional pseudocapacitive charge storage [35, 36] or several intermediate phases with differing active sites for the lithium-ions [37].

In this paper, we report a one-step hydrothermal synthesis of the rutile phase of TiO_2 nanorods, both pristine and Nb-doped, using water as a solvent. Doping of Nb^{5+} into the lattice was confirmed by X-ray diffraction and Rietveld refinement, and the position and orientation of the 1D channels was investigated by HRTEM. Nanoparticles were then applied as the electrode material in a lithium batteries in the form of half-cell configuration and tested for cycle stability and rate retention between 1 to 3 V *vs* Li/Li^+ and between 0.05 to 3 V *vs* Li/Li^+.

2. Experimental section

2.1 Synthesis

All chemicals used in this experiment were used without further purification; 5 mL of technical grade titanium (IV) butoxide (Sigma Aldrich, Garching, Germany), 12.5 mL of deionised water and 12.5 mL of 37% hydrochloric acid (HCl, Sigma Aldrich, Garching,

Germany) were mixed together and stirred until a homogenous mixture was obtained. For the doped sample, 5 at% of -325 mesh (99.8%) niobium powder (Alfa Aesar, Lancashire, UK) was added to the mixture. The whole mixture was then transported into the Parr autoclave and heated up to 180°C for 20 h. After cooling down, the obtained wet powder was washed with water and centrifuged (the washing procedure was repeated until reaching neutral pH), and then dried in air at 70°C.

2.2 Structure and Morphology Characterization

For identification of the crystal structure powder X-ray diffraction (XRD) patterns of the samples were obtained on an STOE diffractometer using Mo-Kα radiation (λ = 0.71 Å) over the 2θ range 5 to 40° with a step size of 0.5° and step time of 30 s. The Rietveld refinement was performed on the collected data using General Structure Analysis System (GSAS) and EXPGUI suite in order to determine the unit cell parameters [38, 39]. Energy dispersive X-ray spectroscopy (EDX- obtained by using a JEOL JSM-6301F Field Emission SEM) was used to determine the Nb:Ti atomic ratio on the carbon-coated samples. Lattice structural information and EDX mapping were examined with a JEOL 2100 TEM. Measurements of surface composition and the state of elements were carried out using a Thermo Scientific K-Alpha X-ray photoelectron spectrometer (XPS) with a monochromatic Al-Kα source. Results were then fitted using CasaXPS^{TM} software with the binding energies suited to carbon (285 eV). Brunauer-Emmett-Teller (BET) surface area measurements were carried out using N_2 in a micrometrics ASAP 2020 Automatic High Resolution Micropore Physisorption Analyzer. The samples were degassed at 70°C (12 h) under vacuum before measurements. Thermogravimetric analysis (TGA) was performed using a TGA Q500 instrument (TA instruments) under nitrogen with a flow rate of 40 mL min^{-1}. The temperature was first increased with 20 ^{o}C min^{-1} to 100 ^{o}C and kept for 10 min for surface water removal (to get the real crystal water content in the electrode). Then the test started from 100 to 600 ^{o}C with a heating rate of 20 ^{o}C min^{-1}.

2.3 Electrochemical Characterization

The nanomaterials were used as electrode active material. The slurry for the electrode was prepared with a content of 70 wt% active material, 20 wt% conductive agent (carbon black, Super P, Alfa Aesar, Heysham, UK) and 10 wt% polyvinylidene fluoride (PVDF, Kynar 761, ARKEMA, King of Prussia, USA). PVDF was dissolved in N-Methyl-2-pyrrolidone (NMP, Sigma Aldrich, St. Louis, USA) for at least 1 hour at room temperature, before adding the active material and conductive agent, which was mixed with a ball mill (30 min, 700 rpm). The slurry was cast on a copper foil and dried in an oven at 70 °C for 1 h and then left overnight at room temperature. Electrodes with a diameter of 15 mm were punched out, pressed (2 tons of force for 30 seconds) and finally dried overnight at 70 °C. The specific electrode mass loading for each electrode disc was between 1.0 to 2.0 mg cm^{-2}.

Electrochemical experiments were performed using a two-electrode 2032-type coin cell, which was assembled in an argon-filled glovebox with O_2 and H_2O limited below 3 ppm (MB150B-G, MBraun, Garching, Germany). The counter electrode was lithium metal foil (Hohsen Corp., Osaka, Japan). The separator (glass microfiber filters, Whatman®, GF/B Buckinghamshire, UK) was saturated with an organic electrolyte of 1 M $LiPF_6$ in EC/DMC (1:1 v/v, Merck Selectipur LP40, Darmstadt, Germany).

Cyclic voltammetry (CV) measurements were performed with a galvanostat / potentiostat (PGSTAT302, AUTOLAB, Metrohm, Utrecht, Netherlands) between 1 to 3 V *vs* Li/Li^+ at 0.1 mV s^{-1} and between 0.05 to 3 V *vs* Li/Li^+ at 0.2 mV s^{-1}. Electrochemical measurements were performed using a MACCOR battery tester (Model 4200, Maccor Inc., Oklahoma, USA) at room temperature. The tests were performed between 1 to 3 V *vs* Li/Li^+ and 0.05 to 3 V *vs* Li/Li^+ with applied currents ranging from 0.05 to 1 A g^{-1}.

3. Results and discussion

3.1 Materials Characterization

Pure rutile TiO_2 was collected as white powder, and Nb doped TiO_2 was collected as light blue powder. The X-ray diffraction patterns of pristine and Nb doped TiO_2 powders revealed the rutile TiO_2 phase in their structures (Figure 2a). In the undoped powder, only reflections associated with the rutile TiO_2 phase were found. In the $Ti_{0.96}Nb_{0.04}O_2$ sample, in addition to the rutile TiO_2 phase, two peaks in the 10-12° 2θ range were observed, which might belong to a secondary phase of $TiNb_2O_7$. It has been omitted from further analysis as the intensity of the peaks is nearly negligible compared to the intensity of the rutile peaks.

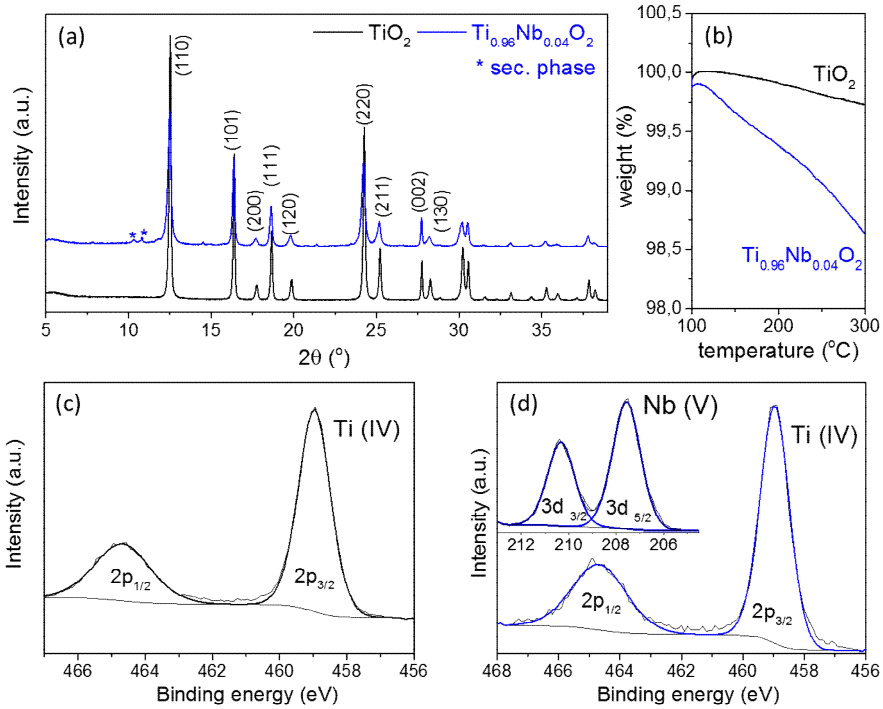

Figure 2. (a) XRD pattern of pristine and Nb-doped rutile TiO_2. The rutile reflection positions with appropriate values (*h k l*) are shown in brackets. (b) TGA analysis for each sample. XPS spectra of (c) pristine TiO_2 and (d) $Ti_{0.96}Nb_{0.04}O_2$ nanoparticles in the titanium 2p region (insert shows the niobium 3d region).

In supplementary Figure S1, a pattern shift at higher 2θ angles is shown. TGA analysis showed an increased crystal water content for the doped sample with less than 0.2 wt% for pristine TiO_2 and *ca.*

1.4 wt% for doped TiO_2 (given that crystal water can be removed up until 300 ^oC).

The Rietveld refinement was used to obtain the unit cell parameters and to determine if an expansion in the unit cell volume occurs when doped with niobium. The lattice constants in pristine TiO_2 were a = 4.5906 Å and c = 2.9557 Å and increased upon niobium doping into the system to a = 4.6058 Å and c = 2.9594 Å. Unit cell volume therefore increases from 62.29 $Å^3$ for undoped TiO_2 to 62.78 $Å^3$ for $Ti_{0.96}Nb_{0.04}O_2$.

sample	a (Å)	b (Å)	c (Å)	Unit cell volume ($Å^3$)	R_{wp} (%)	BET surface area ($m^2\ g^{-1}$)
TiO_2	4.5906(58)	4.5906(58)	2.9557(33)	62.29	5	10.0
$Ti_{0.96}Nb_{0.04}O_2$	4.6058(51)	4.6058(51)	2.9594(32)	62.78	8	46.2

Table 1. The effect of increasing Nb content and surface area measurements on lattice parameters *a, b* and *c*. The lattice parameters were obtained from Rietveld refinement fitting of models to the data. The associated fitted R_{wp} for the goodness of fit is also given; below 8% indicates a good fit.

X-ray photoelectron spectroscopy was performed on both as-synthesised samples (pristine TiO_2 and $Ti_{0.96}Nb_{0.04}O_2$). For the pristine TiO_2 sample the binding energy for the Ti $2p_{3/2}$ excitation is 458.9 eV, which corresponds with Ti^{4+} in TiO_2 (Figure 2b). $Ti_{0.96}Nb_{0.04}O_2$ rutile powders showed primarily Ti^{4+} species with binding energies of 458.9 and 464.7 eV for $2p_{3/2}$ and $2p_{1/2}$ respectively. Niobium in the $Ti_{0.96}Nb_{0.04}O_2$ powder only fitted the Nb^{5+} oxidation state, with binding energies of 207.6 and 210.4 eV for $3d_{5/2}$ and $3d_{3/2}$ respectively; though the lack of the Nb^{4+} $3d_{5/2}$ and Ti^{3+} $2p_{3/2}$ transitions might be due to detection limit of XPS (Figure 2c). Semi-quantitative analysis of the peak areas of the Ti(2p) and Nb(3d) core lines estimated the elemental composition at the surface to be 4.5 at% Nb relative to Ti.

In Figure 3, the SEM results are presented. Similar to the literature [40-42], the synthesized rutile nanorods seemed to orient in a micro-structured spherical cluster. The SEM images of the prepared electrodes showed that the microspherical particles made of nanorods were partly

cracked during electrode processing, possibly enabling more lithium-ion entrance sites (supplementary Figure S2).

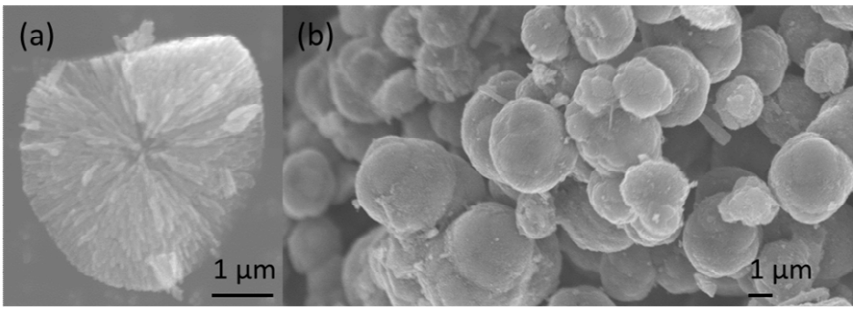

Figure 3. SEM image of (a) pristine TiO_2, (b) $Ti_{0.96}Nb_{0.04}O_2$.

High resolution TEM analysis was performed on both samples (Figure 4a,b). Pristine TiO_2 powder consisted only of rutile rods with sizes varying from 100 nm to 1.5 µm in length. In the $Ti_{0.96}Nb_{0.04}O_2$ powder the only phase to be found is rutile, forming characteristic rods, minor impurities of other phases visible in XRD pattern has not been detected by TEM. Similar to the pristine TiO_2 powder, the main reflections found in all the investigated rods were from the (111) and (110) planes, suggesting growth in this particular crystal orientation only. Moreover, all of the investigations of HRTEM crystals showed that the (110) plane was orientated along the longer edge of the crystal for both pristine and doped samples. As the lithium-ion diffusion coefficient along the *c*-axis is 9 orders of magnitude higher than that of the *ab*-plane, such orientation is essential to achieve effective charging/discharging. Measurement of the diameters of all the investigated rods showed that diameters ranged between 20 and 300 nm in the undoped powder and from 6 to 40 nm in the Nb-doped powder.

EDX mapping and elemental analysis results show that for a 5% Nb solution, 3.5% is incorporated into the powder structure (sample $Ti_{0.96}Nb_{0.04}O_2$), Figure 4c. Elemental mapping of the $Ti_{0.96}Nb_{0.04}O_2$ powder shows that both Nb and Ti are evenly distributed in the particle. Overall, the colour change of the powder, unit cell volume changes and EDX mapping show a

successful doping of Nb^{5+} in the rutile TiO_2 lattice. The BET surface area was 10.04 m^2 g^{-1} for pure TiO_2 and 46.19 m^2 g^{-1} for $Ti_{0.96}Nb_{0.04}O_2$.

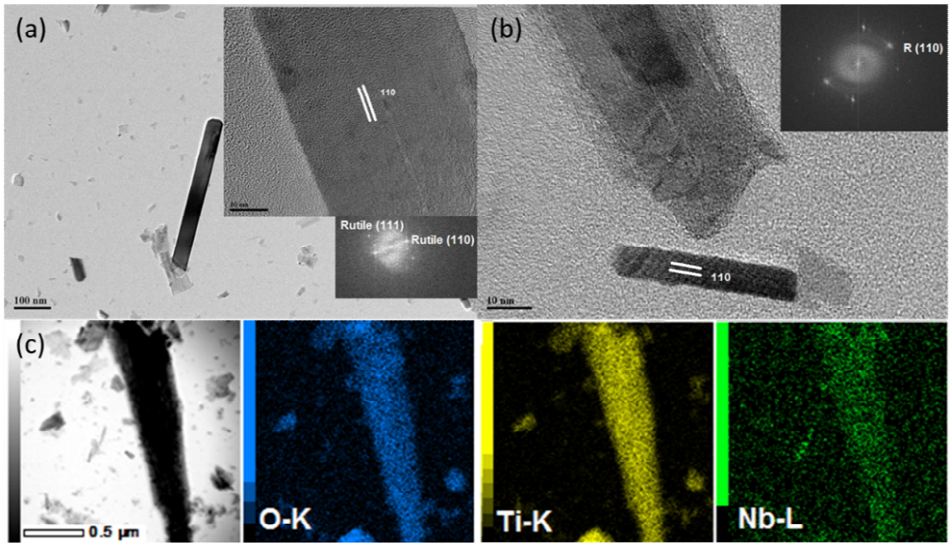

Figure 4. TEM image of (a) pristine TiO_2, (b) $Ti_{0.96}Nb_{0.04}O_2$. (c) Elemental mapping of $Ti_{0.96}Nb_{0.04}O_2$: O (blue), Ti (yellow) and Nb (green).

Since the radius of Nb^{5+} is 0.03 Å bigger than the Ti^{4+}, it generates a stress upon substitutional incorporation into the TiO_2 lattice, causing an inhibition of the growth of the TiO_2 crystallites, as described by Sharma *et al.* [43], which explains the increase of the surface area of doped TiO_2. As shown by Burnside *et al*. the surface area of the TiO_2 particles synthesized in the autoclave varies from 10 to 50 m^2 g^{-1}, depending on the temperature of the process [44].

Overall, doping TiO_2 with Nb increased the unit cell volume and the atomic distances as shown by the Rietveld refinement. In practice, doping Nb widens the channels for the lithium-ion exchange. Moreover, doping Nb can be used to drastically decrease the particle size and increase the surface area, which is known to benefit lithium-ion battery negative electrode performance for rutile TiO_2.

3.2 Electrochemical Performance between 1-3 V *vs* Li/Li^+

In literature, rutile phase of TiO_2 is generally tested in the potential window of 1-3 V *vs* Li/Li^+ because of the reversible redox activity of Ti^{4+}/Ti^{3+} in this range. The cyclic voltammetry plot for this potential range is presented in Figure 5a and the galvanostatic charge / discharge

cycling plot is presented in Figure 5b. As mentioned previously, the first domain (between 3 to *ca.* 1.4 V *vs* Li/Li^+) refers to the surface storage of lithium-ions. Consequently, the region was only observed for the higher surface area Nb-doped material (46.2 m^2 g^{-1}) and not distinct for the pure rutile TiO_2 material (10 m^2 g^{-1}). As a result, only 19 mAh g^{-1} (0.06 M lithium-ions) was stored in pure rutile TiO_2 while 200 mAh g^{-1} (0.6 M lithium-ions) was stored in the Nb-doped TiO_2 between 3 to 1.4 V *vs* Li/Li^+ (Figure 4b). $Ti_{0.96}Nb_{0.04}O_2$ showed higher lithium-ion insertion performance in the second domain (*ca.* 1.4 to 1.1 V *vs* Li/Li^+) indicating that smaller particle size (see TEM) and broader *c*-channels (see Table 1) reduced the impact of blocked channels and lithium-ion diffusion limitations compared to pure rutile TiO_2.

During delithiation, there was only one broad deinsertion peak (1.8 V *vs* Li/Li^+) for undoped rutile TiO_2 and two peaks (1.8 and 2.6 V *vs* Li/Li^+) for doped TiO_2 (Figure 4a). The slight delithiation peak at 2.6 V *vs* Li/Li^+ (Nb-doped TiO_2) is very unusual and will be discussed further in the next section (cycling between 0.05 to 3 V *vs* Li/Li^+). Each delithiation profile for cycles 2-5 was highly reversible indicating reversible lithium-ion electrochemical activity after the first cycle which is also reflected in the constant capacities for each material in Figure 5b.

Some reports have claimed initial maximum insertion of 0.85 M (285 mAh g^{-1}) lithium-ions into the rutile TiO_2 nanomaterial [20, 21, 29]. In this paper we present an initial insertion of 0.92 M (310 mAh g^{-1}) for pure rutile TiO_2 and 1.19 M (410 mAh g^{-1}) of lithium-ions for $Ti_{0.96}Nb_{0.04}O_2$ (Figure 5b), which is not unlikely given that Usui *et al.* observed an initial insertion of 1.34 M (450 mAh g^{-1}) lithium-ions into rutile $Ti_{0.94}Nb_{0.06}O_2$ [45].

In Figure 5c, a current rate test followed by long term cycling is presented. During the first cycle, the Coulombic efficiency at 50 mA g^{-1} was *ca.* 43.5% and 56.1% for pure and doped rutile TiO_2, respectively. The measured specific delithiation capacities were 104 and 167 mAh g^{-1} at 50 mA g^{-1}, 54 and 115 mAh g^{-1} at 250 mA g^{-1}, 34 and 94 mAh g^{-1} at 500 mA g^{-1} and 27 and 76 mAh g^{-1} at 1000 mA g^{-1} for pure and doped rutile TiO_2, respectively.

The Coulombic efficiency was *ca.* 98.5% and 95% at 50 mA g^{-1} and above 99% at higher currents for pure and doped rutile TiO_2, respectively. The low Coulombic efficiency at 50 mA g^{-1} for high surface area rutile TiO_2 has been observed before [22].

A large change in unit cell volume, most likely caused by continual mechanical failure of the pristine microsized particles, leads to smaller crystallites during cycling [21, 29]. This breaking up the larger crystallites of the pure rutile TiO_2 particles could be a reason for the increasing capacity during long term cycling by exposing more active lithium ion sites (see cycle 50 to 150).

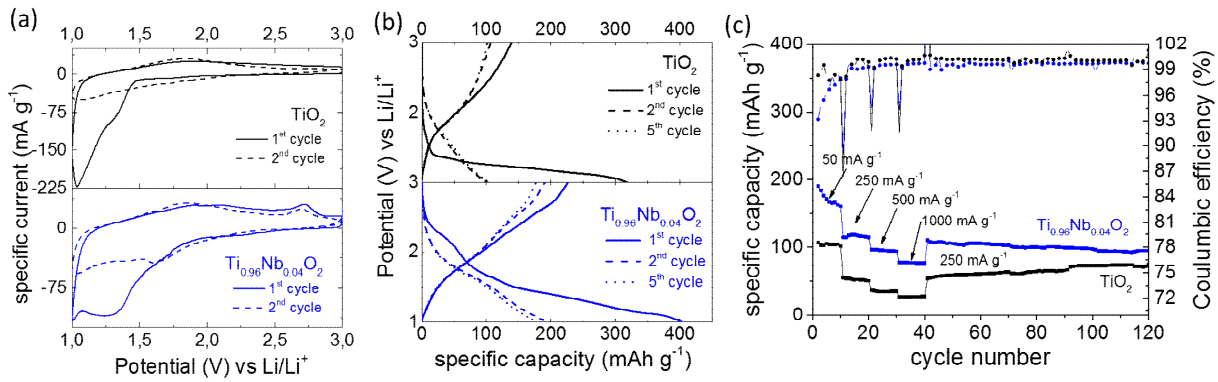

Figure 5. Presentation of the initial cycles tested *via* potentiodynamic and galvanostatic methods between 1-3 V *vs* Li/Li^+: (a) CV at 0.1 mV s^{-1} and (b) galvanostatic charge / discharge cycling at an applied current of 50 mA g^{-1}. (c) C rate test at various current rates with followed long term cycling at 250 mA g^{-1}.

In order to understand the reactions occurring herein, ex-situ XRD experiments were performed for cycled electrodes after one cycle between 1-3 V *vs* Li/Li^+ at 50 mA g^{-1} for the delithiated stage (Figure 6). The crystalline structure was destroyed for both materials indicated by the lower rutile pattern intensities [21, 29]. For both samples, there was a change of pattern intensity and broadening at $2\theta = 19.7$ ° and at $2\theta = 27.9$ ° (see shaded red area in Figure 6). In the literature, this was suggested to belong to the hexagonal or monoclinic $LiTiO_2$ [21, 28, 29]. But to date, there is no understanding where, whether within the single particle or

electrode or why this phase is formed irreversibly for rutile TiO_2 electrode materials. There was also an indication of another phase for the Nb-doped TiO_2 as shown by the star with a shoulder at $2\theta = 16.5$ °. This might be explained by the fact that Nb-doping into the rutile TiO_2 lattice creates thermodynamically metastable solid solutions [46-49].

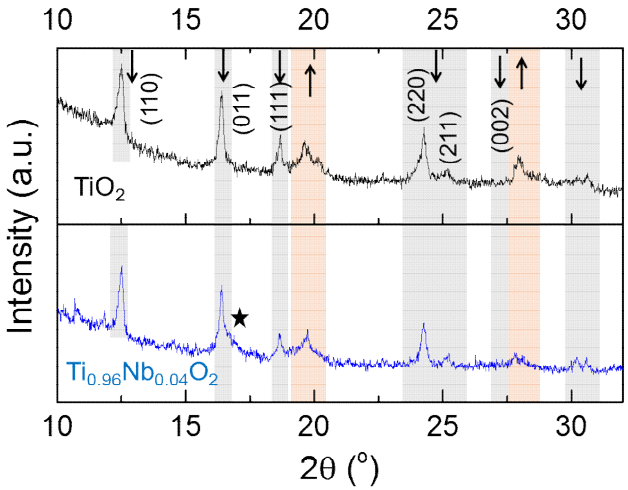

Figure 6. Ex-situ XRD of the cycled electrode material after one cycle between 1 to 3 V *vs* Li/Li^+ (delithiated stage). The grey area shows the decreased pattern intensity for rutile TiO_2 and the red area indicates the increased patterns of a $LiTiO_2$ phase. The star indicates an additional pattern change for Nb-doped TiO_2.

In Table 2, the electrochemical performance of various rutile TiO_2 materials from the literature are compared to the two materials synthesized in this work. The cell parameters of the unit cells show that the slight differences occurred predominately in the *a/b* plane and less in the *c* plane when nanosizing. As mentioned before, a main barrier for lithium-ion insertion into rutile TiO_2, is the low lithium-ion diffusion in *a/b* direction, making the diffusion one dimensional. The increased distance in *a/b* direction might improve this diffusion limitation. Reddy *et al*. showed drastic increased lithium-ion uptake when Nb is doped into microsized rutile TiO_2 [50]. But surely more importantly, nano-sizing and the natural morphology of the rod-type structure results in higher lithium-ion insertion entrances to the host material facing towards the electrolyte, see HRTEM with (110) plane (Figure 3b). This can drastically reduce the impact of blockages in the *c*-channels. All materials with higher surface areas showed

higher capacities compared to the materials presented herein, showing again the huge impact of particle size compared to unit cell expansion.

rutile material	a (Å) = b (Å)	c (Å)	surface area (m^2 g^{-1})	specific capacity (mAh g^{-1})	ref.
TiO_2	4.5906(58)	2.9557(33)	10	100 @50 mA g^{-1}	
$Ti_{0.96}Nb_{0.04}O_2$	4.6058(51)	2.9594(32)	46	167 @50 mA g^{-1}	
bulk-TiO_2	**4.5929 (4)**	**2.9596 (4)**	**/**	**30 @30 mA g^{-1}**	**[20]**
nano-rod-TiO_2	4.610 (3)	2.956 (2)	/	150 @30 mA g^{-1}	[20]
nano-needles TiO_2	4.593	2.959	181	190 @67 mA g^{-1}	[51]
nano-$Ti_{0.94}Nb_{0.06}O_2$	4.608	2.956	/	215 @167 mA g^{-1}	[45]
nano-TiO_2	4.61230	2.95247	/	118 @17 mA g^{-1}	[52]
hydrogenated nano-TiO_2	4.61107	2.97147	/	180 @17 mA g^{-1}	[52]
nano-rod-TiO_2	/	/	106.1	170 @33 mA g^{-1}	[53]
urchin-like nano-TiO_2	/	/	80	220 @335 mA g^{-1}	[54]
nano-TiO_2	/	/	112	200 @335 mA g^{-1}	[55]
cauliflower-like rutile TiO_2	/	/	180	183 @67 mA g^{-1}	[30]

Table.2. Comparison of rutile TiO_2 materials from the literature with the materials from this work. The lattice parameters, surface area and electrochemical performances are compared.

The decreased particle size is the main contributor towards the improved electrochemical performance of sample $Ti_{0.96}Nb_{0.04}O_2$. Consequently, doping with Nb^{5+} using the synthesis method herein prevents crystal growth of TiO_2 resulting in smaller particle size. Summing up, nanosizing with c-channels showing to the surface and doping for improved lithium-ion diffusion should result in optimized electrochemical performance for rutile TiO_2 electrode materials.

3.3 Electrochemical Performance between 0.05-3 V *vs* Li/Li^+

There have recently been several reports which show the potential for additional electrochemical activity at a wider potential window for nanosized materials [35, 36]. During lithiation, one major difference between the two samples was the plateau observed at 0.6 V *vs* Li/Li^+ (Figure 7a), see also supplementary Figure S3 which shows the role of the carbon black

on this plateau. In general, the solid electrolyte interface (SEI) formation can be expected for this potential range [56], but the broadness and intensity of the lithium-ion insertion plateau was far higher for the doped sample and shifted reversibly towards 0.75 V *vs* Li/Li^+ for the next cycles, showing additional lithium-ion storage sites in the structure for Nb-doped TiO_2. During delithiation, the profile of the pure rutile TiO_2 showed a broad delithiation plateau at 1.8 V *vs* Li/Li^+ (Figure 7b). The doped sample showed overall four reversible delithiation plateaus (*ca.* 0.9, 1.25, 1.7 and 2.6 V *vs* Li/Li^+). Compared to cycling between 1 to 3 V *vs* Li/Li^+, the delithiation plateau at 2.6 V *vs* Li/Li^+ drastically increased and the peak at 1.7 V *vs* Li/Li^+ became more resolved when cycled in the wider potential range which may show a correlation of phase changes at lower potentials. Additionally, the peak at 2.6 V *vs* Li/Li^+ might (partly) relate to the decomposition and oxidization of the previously formed SEI (this would also explain, why the peak increased when cycling down to 0.05 V compared to 1 V *vs* Li/Li^+), which was seen by others for SnO_2 based materials [57, 58].

The four reversible delithiation plateaus within this study for Nb-doped rutile TiO_2 (*ca.* 0.9, 1.25, 1.7 and 2.6 V *vs* Li/Li^+) were unique for titanate based materials. In 1999, Irvine *et al.* showed that there was a drastic difference in lithium-ion insertion behavior depending on the structure and size of the material for ramsdellite and spinel titanate based materials. A higher lithium-ion insertion/de-insertion activity at 2.3 V *vs* Li/Li^+ was attributed to the decreased particle size, resulting in higher ion diffusion, and specific structure [37]. Moreover, it could be concluded that the unique insertion / de-insertion behavior may indicate several intermediate phases, perhaps with differing side occupants [37]. Maier *et al.* showed in several works a dependence on surface area and different energy levels (potentials) for lithium-ion uptake [21, 59]. However, the capacity remained stable after the second cycle which shows a stable cycling stability (see Figure 7b).

In Figure 6a, a current rate test with followed long term cycling is presented. The first cycle Coulombic efficiency at 50 mA g^{-1} was *ca.* 47% and 54% for pure and doped rutile TiO_2,

respectively. The measured specific delithiation capacities were 380 and 215 mAh g^{-1} at 50 mA g^{-1}, 305 and 170 mAh g^{-1} at 250 mA g^{-1}, 275 and 150 mAh g^{-1} at 500 mA g^{-1} and 234 and 127 mAh g^{-1} at 1000 mA g^{-1} (for pure and doped rutile TiO_2, respectively). The galvanostatic charge / discharge profiles at each current rate are presented in the supplementary Figure S4. The Coulombic efficiency was *ca.* 98% and 94% at 50 mA g^{-1} and above 98.5% at higher currents for pure and doped rutile TiO_2, respectively. Moreover, the doped sample showed a stable capacity of 402 mAh g^{-1} after 100 cycles at 100 mA g^{-1} (supplementary Figure S5).

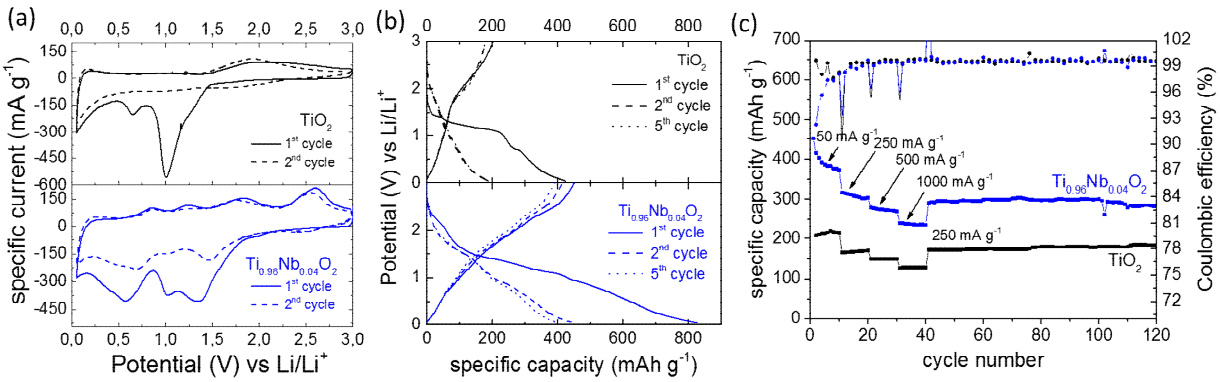

Figure 7. Presentation of the initial cycles tested *via* potentiodynamic and galvanostatic methods between 0.05-3 V *vs* Li/Li^+: (a) CV at 0.2 mV s^{-1} and (b) galvanostatic charge / discharge cycling at an applied current of 50 mA g^{-1}. (c) C rate test at various current rates with followed long term cycling at 250 mA g^{-1}.

Ex-situ XRD experiments were performed for cycled electrodes after one cycle between 0.05-3 V *vs* Li/Li^+ at 50 mA g^{-1}, at a de-lithiated stage (Figure 8). Similar to cycling between 1-3 V *vs* Li/Li^+, the crystallite size decreased for both materials. For both samples, there was a change of pattern intensity and broadening at 2θ = 19.7 ° and at 2θ = 27.9 ° (see shaded red area in Figure 8), indicating again a mixed phase of rutile TiO_2 and $LiTiO_2$. The new phase that was identified in Figure 6 for the Nb-doped TiO_2 with a star at 2θ = 16.5° is more visible after cycling in this boarder potential range. Most likely, Nb-doping can render this unknown phase

more stable during cycling (see peak intensities). Unlike the pure TiO_2, the (011) pattern displayed higher intensity compared to the (110) pattern for the Nb-doped TiO_2. Moreover, there were additional patterns at *ca.* 2θ = 16.5 °, 20.4 ° and at 26.7 ° (due to the high noise to signal ratio, a proper phase identification was not possible). This increased phase intensity may also be indicative of the additional lithium-ion storage sites in the Nb-doped electrode material. Therefore, the some of the additional lithium-ion de-lithiation peaks in the CV might arise from this phase change (Figure 7a).

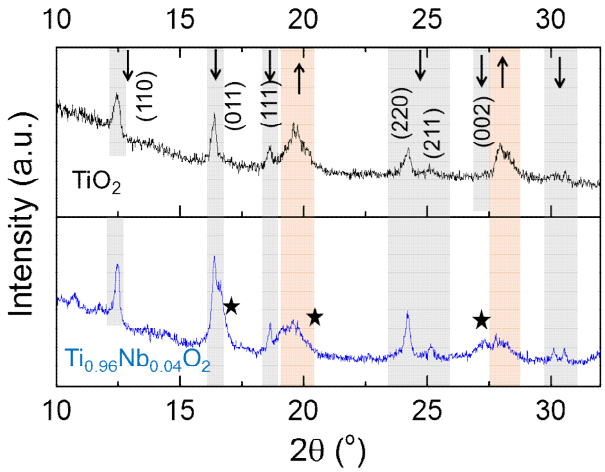

Figure 8. Ex-situ XRD of the cycled electrode material after one cycle between 0.05 to 3 V *vs* Li/Li^+ (delithiated stage). The grey area indicates decreased pattern intensity for rutile TiO_2 and the red area indicates the increased patterns of a $LiTiO_2$ phase. The star shows an additional pattern change for Nb-doped TiO_2.

Even if the broad operational potential range (used in this work) is not practical for a full cell lithium-ion battery, where a sharp lithium-ion insertion / de-insertion at low potentials is favored, the results still show a gap in the knowledge of nanosized titanate based electrode materials in considering the proportion of lithium-ions that can actually be inserted and de-inserted in titanate based electrodes. In comparison with the majority of literature, the obtained capacities are higher for any pure rutile titanate based negative electrode material with 390 mAh g^{-1} at 50 mA g^{-1} after 100 cycles (Figure 3b). Wohlfahrt-Mehrens *et al.* investigated the temperature behavior of rutile TiO_2 (0.1 to 3 V *vs* Li/Li^+)

with a surface area of 180 m^2 g^{-1} at 67 mA g^{-1} with reversible capacities around 350 mAh g^{-1} [30]. Our phase pure rutile TiO_2 showed the same behavior as reported in literature between *ca.* 0.1 to 3 V *vs* Li/Li^+. Firework-shaped rutile TiO_2 with a surface area of 76.4 m^2 g^{-1} showed reversible capacities around 177 mAh g^{-1} at 100 mA g^{-1} after 200 cycles [31]. Rutile TiO_2 microspheres with surface area of 58.4 m^2 g^{-1} showed reversible capacities around 126 mAh g^{-1} at 100 mA g^{-1} after 100 cycles [32]. Rutile TiO_2 nanocrystals with surface area of 81.9 m^2 g^{-1} showed reversible capacities around 102 mAh g^{-1} at 500 mA g^{-1} after 100 cycles [33] and rutile TiO_2 nanobundles on reduced graphene showed reversible capacities around 300 mAh g^{-1} at 200 mA g^{-1} after 500 cycles [34]. Unfortunately, most of the aforementioned reports did not give a discussion about the additional charge storage at low potentials or showed cyclic voltammetry measurements at low scan rates thus limiting a comparison of the electrochemical activity.

Overall, the insertion / deinsertion behavior showed a unique electrochemical behavior for $Ti_{0.96}Nb_{0.04}O_2$ resulting in high reversible capacities. The nature of the lithium-ion uptake and release is still not fully understood and requires further investigation.

4. Conclusions

Undoped and Nb-doped rutile TiO_2 nanorods were synthesized *via* a one-step hydrothermal method. Doping with Nb^{5+} was shown to alter the orientation of the 1D channels promoting improved lithium-ion uptake during cycling. The surface area could be increased *via* doping, which is known to benefit the charge storage properties. The synthesized materials were investigated as possible negative electrode materials for lithium-ion batteries and tested between 1 to 3 V *vs* Li/Li^+ and between 0.05 to 3 V *vs* Li/Li^+. The Nb-doped sample showed superior performance with 167 and 104 mAh g^{-1} for 1 to 3 V *vs* Li/Li^+ and 380 and 215 mAh g^{-1} for 0.05 to 3 V *vs* Li/Li^+ (at 50 mA g^{-1} for doped and undoped TiO_2, respectively). The increased charge storage properties was attributed to differing phase changes during lithiation and de-lithiation for doped and undoped TiO_2 offering/which offered increased lithium-ion active sites

Acknowledgement

The EPSRC are thanked for funding the Centre for Doctoral Training in Molecular Modelling & Materials Science (UCL, UK) and A*Star (Singapore) are thanked for supporting a studentship for AJG and ML. AJG thanks Mr Fadly Rosman for his drawing.

References

[1] M. Winter, R.J. Brodd, Chemical reviews, 104 (2004) 4245-4270.
[2] M.R. Palacin, Chemical Society Reviews, 38 (2009) 2565-2575.
[3] L. Ji, Z. Lin, M. Alcoutlabi, X. Zhang, Energy & Environmental Science, 4 (2011) 2682-2699.
[4] Z. Yang, J. Zhang, M.C. Kintner-Meyer, X. Lu, D. Choi, J.P. Lemmon, J. Liu, Chemical Reviews, 111 (2011) 3577-3613.
[5] K. Saravanan, P. Balaya, M. Reddy, B. Chowdari, J.J. Vittal, Energy & Environmental Science, 3 (2010) 457-463.
[6] L. Wang, X. He, W. Sun, J. Wang, Y. Li, S. Fan, Nano letters, 12 (2012) 5632-5636.
[7] K. Byrappa, T. Adschiri, Progress in Crystal Growth and Characterization of Materials, 53 (2007) 117-166.
[8] M. Yoshimura, K. Byrappa, Journal of Materials Science, 43 (2008) 2085-2103.
[9] A. Rabenau, Angewandte Chemie International Edition in English, 24 (1985) 1026-1040.
[10] G. Demazeau, Journal of Materials Chemistry, 9 (1999) 15-18.
[11] A. Kafizas, C.W. Dunnill, I.P. Parkin, Journal of Materials Chemistry, 20 (2010) 8336-8349.
[12] M.-A. Einarsrud, T. Grande, Chemical Society Reviews, 43 (2014) 2187-2199.
[13] A. Yoshino, Angewandte Chemie International Edition, 51 (2012) 5798-5800.
[14] O.W. Johnson, Physical Review, 136 (1964) A284-A290.
[15] M.V. Koudriachova, N.M. Harrison, S.W. de Leeuw, Solid State Ionics, 157 (2003) 35-38.
[16] M.V. Koudriachova, N.M. Harrison, S.W. de Leeuw, Physical Review B, 65 (2002) 235423.
[17] M.V. Koudriachova, N.M. Harrison, S.W. de Leeuw, Physical review letters, 86 (2001) 1275.
[18] A. Stashans, S. Lunell, R. Bergström, A. Hagfeldt, S.-E. Lindquist, Physical Review B, 53 (1996) 159.
[19] Z. Yang, D. Choi, S. Kerisit, K.M. Rosso, D. Wang, J. Zhang, G. Graff, J. Liu, Journal of Power Sources, 192 (2009) 588-598.
[20] E. Baudrin, S. Cassaignon, M. Koelsch, J.P. Jolivet, L. Dupont, J.M. Tarascon, Electrochemistry Communications, 9 (2007) 337-342.
[21] Y.S. Hu, L. Kienle, Y.G. Guo, J. Maier, Advanced Materials, 18 (2006) 1421-1426.
[22] C. Jiang, I. Honma, T. Kudo, H. Zhou, Electrochemical and solid-state letters, 10 (2007) A127-A129.
[23] B.N. Joshi, H. Yoon, M.F. Hest, S.S. Yoon, Journal of the American Ceramic Society, 96 (2013) 2623-2627.
[24] D.O. Scanlon, C.W. Dunnill, J. Buckeridge, S.A. Shevlin, A.J. Logsdail, S.M. Woodley, C.R.A. Catlow, M.J. Powell, R.G. Palgrave, I.P. Parkin, Nature materials, 12 (2013) 798-801.
[25] P. Hasin, M.A. Alpuche-Aviles, Y. Li, Y. Wu, The Journal of Physical Chemistry C, 113 (2009) 7456-7460.

[26] D. Wang, D. Choi, Z. Yang, V.V. Viswanathan, Z. Nie, C. Wang, Y. Song, J.-G. Zhang, J. Liu, Chemistry of Materials, 20 (2008) 3435-3442.
[27] S.J. Kim, S.-Y. Noh, A. Kargar, D. Wang, G.W. Graham, X. Pan, Chemical Communications, 50 (2014) 9932-9935.
[28] M.A. Reddy, M.S. Kishore, V. Pralong, V. Caignaert, U.V. Varadaraju, B. Raveau, Electrochemistry Communications, 8 (2006) 1299-1303.
[29] W.J. Borghols, M. Wagemaker, U. Lafont, E.M. Kelder, F.M. Mulder, Chemistry of Materials, 20 (2008) 2949-2955.
[30] M. Marinaro, M. Pfanzelt, P. Kubiak, R. Marassi, M. Wohlfahrt-Mehrens, Journal of Power Sources, 196 (2011) 9825-9829.
[31] B. Guo, K. Yu, H. Fu, Q. Hua, R. Qi, H. Li, H. Song, S. Guo, Z. Zhu, Journal of Materials Chemistry A, 3 (2015) 6392-6401.
[32] S. Guo, J. Liu, S. Qiu, Y. Wang, X. Yan, N. Wu, S. Wang, Z. Guo, Electrochimica Acta, 190 (2016) 556-565.
[33] Y. Li, Y. Hu, J. Shen, H. Jiang, G. Min, S. Qiu, Z. Song, Z. Sun, C. Li, Nanoscale, 7 (2015) 18603-18611.
[34] M. Zhen, X. Guo, G. Gao, Z. Zhou, L. Liu, Chemical Communications, 50 (2014) 11915-11918.
[35] M. Lübke, P. Marchand, D.J. Brett, P. Shearing, R. Gruar, Z. Liu, J.A. Darr, Journal of Power Sources, 305 (2016) 115-121.
[36] M. Lübke, A. Sumboja, I.D. Johnson, D.J. Brett, P.R. Shearing, Z. Liu, J.A. Darr, Electrochimica Acta, 192 (2016) 363-369.
[37] R.K. Gover, J.R. Tolchard, H. Tukamoto, T. Murai, J.T. Irvine, Journal of the Electrochemical Society, 146 (1999) 4348-4353.
[38] B.H. Toby, Journal of applied crystallography, 34 (2001) 210-213.
[39] A.C. Larson, R.B. Von Dreele, General Structure Analysis System. LANSCE, MS-H805, Los Alamos, New Mexico, (1994).
[40] R. Gao, Z. Jiao, Y. Wang, L. Xu, S. Xia, H. Zhang, Chemical Engineering Journal, 304 (2016) 156-164.
[41] H. Fei, M. Wei, Electrochimica Acta, 56 (2011) 6997-7004.
[42] Y. Zhang, X. Pu, Y. Yang, Y. Zhu, H. Hou, M. Jing, X. Yang, J. Chen, X. Ji, Physical Chemistry Chemical Physics, 17 (2015) 15764-15770.
[43] R.K. Sharma, M. Bhatnagar, Sensors and Actuators B: Chemical, 56 (1999) 215-219.
[44] S.D. Burnside, V. Shklover, C. Barbé, P. Comte, F. Arendse, K. Brooks, M. Grätzel, Chemistry of materials, 10 (1998) 2419-2425.
[45] H. Usui, S. Yoshioka, K. Wasada, M. Shimizu, H. Sakaguchi, ACS Applied Materials & Interfaces, 7 (2015) 6567-6573.
[46] A. Chaudhary, M.P. Nag, N. Ravishankar, T. Thomas, M. Jain, S. Raghavan, Journal of Physical Chemistry C, 118 (2014) 29788-29795.
[47] D.A. Hanaor, M.H. Assadi, S. Li, A. Yu, C.C. Sorrell, Computational Mechanics, 50 (2012) 185-194.
[48] J. Arbiol, J. Cerda, G. Dezanneau, A. Cirera, F. Peiro, A. Cornet, J.R. Morante, Journal of Applied Physics, 92 (2002) 853-861.
[49] J. Su, Z. Li, Y. Zhang, Y. Wei, X. Wang, RSC Advances, 6 (2016) 16177-16182.
[50] M.A. Reddy, U. Varadaraju, Journal of The Electrochemical Society, 161 (2014) A149-A153.
[51] M. Pfanzelt, P. Kubiak, M. Fleischhammer, M. Wohlfahrt-Mehrens, Journal of Power Sources, 196 (2011) 6815-6821.
[52] J. Qiu, S. Li, E. Gray, H. Liu, Q.-F. Gu, C. Sun, C. Lai, H. Zhao, S. Zhang, The Journal of Physical Chemistry C, 118 (2014) 8824-8830.
[53] H. Qiao, Q. Luo, Q. Wei, Y. Cai, F. Huang, Ionics, 18 (2012) 667-672.
[54] J.S. Chen, Y.N. Liang, Y. Li, Q. Yan, X. Hu, ACS applied materials & interfaces, 5 (2013) 9998-10003.
[55] J.S. Chen, X.W. Lou, Journal of Power Sources, 195 (2010) 2905-2908.
[56] M. Shirpour, J. Cabana, M. Doeff, Energy & Environmental Science, 6 (2013) 2538-2547.

[57] H. Song, N. Li, H. Cui, C. Wang, Journal of Materials Chemistry A, 1 (2013) 7558-7562.
[58] J. Yang, L. Xi, J. Tang, F. Chen, L. Wu, X. Zhou, Electrochimica Acta, 217 (2016) 274-282.
[59] O. Delmer, P. Balaya, L. Kienle, J. Maier, Advanced Materials, 20 (2008) 501-505.